

# Chapter 2.

## BROS: the admittance-controlled multiplayer haptic robot

---

Niek Beckers, Koen Heuver, Arvid Keemink,  
Edwin van Asseldonk, and Herman van der Kooij

**Manuscript in preparation**

## Abstract

Robotic manipulanda facilitate investigations on how two or more humans physically interact when performing a movement task together. Here we describe BROS, a robotic setup with two planar manipulanda designed specifically for studying physical human-human interaction. The design is based on a 5R closed-loop parallel pantograph and was optimized for low end-point mass. Control of each robotic device was implemented using an admittance controller, allowing isotropic dynamic behavior across the workspace. Furthermore, admittance control allows for stable coupling of the two manipulanda and a wide range of haptic interaction conditions. We evaluated the robotic devices in terms of stiffness rendering capabilities, force production, closed-loop position tracking performance and admittance rendering performance. We tested multiple degrees of virtual stiffness up to  $400 \text{ N m}^{-1}$ , however higher stiffness rendering is possible, and the robots can produce over 50 N at the endpoint. The closed-loop position tracking bandwidth to the  $-3 \text{ dB}$  point is approximately 21 Hz. The desired virtual mass-damper admittance could be rendered within a 10 % modulus deviation up to a frequency of 7.5 Hz. Finally, we validated the experimental capabilities of BROS with a human-human interaction experiment in which we varied the stiffness between the two interacting partners.

## 2.1. Introduction

Haptic robotic manipulanda are indispensable tools in studying human motor control, motor learning, physical rehabilitation and physical human-robot interaction. These robots range from lower-extremity exoskeletons, such as the LOPES [1], and full arm exoskeletons, like the ARMIN [2], to one degree of freedom (DOF) devices such as the Hi5 wrist manipulator [3]. Because many aspects of motor control can be studied using arm movements in a plane, most motor control studies predominantly used planar robotic manipulanda with a handle at the endpoint. Examples of planar robotic manipulanda include the vBOT [4], KINARM [5], Braccio di Ferro [6], PFM [7], Haptic Master [8] and 3DOM [9]. Planar endpoint robotic manipulanda have low complexity compared to multi-DOF devices like exoskeletons, allow for high-precision movement sensing and can provide a wide range of dynamic behaviors, such as minimal resistance to movement (e.g., low apparent impedance), rendering stiff objects or applying a velocity-dependent force field.

The existence of planar and similar robotic manipulanda facilitated the research on physical interaction between two humans (e.g. [10–13]). By studying the motor behavior when two partners are physically coupled to each other, for instance when carrying a table together, other researchers and we intend to determine the underlying mechanisms of physical interaction between two humans. One of the advantages of using robotic manipulanda for studying human-human interaction is the flexibility in generating different types of dynamic conditions, such as different physical connections between the interacting partners, ranging from rigid connections (carrying a table together) to compliant connections (for instance two people holding a rubber band).

Most robotic setups used in physical human-human interaction studies consist of two identical robotic manipulanda [3, 10, 14] whose endpoints can be virtually connected through the control software, similar to robotic setups used for bimanual control (e.g. [15]). For instance, Melendez-Calderon et al. [3] developed the Hi5 interface, which is a robotic setup with two 1 DOF wrist manipulanda, one for each partner, that allows wrist flexion and extension. While a dual 1 DOF robotic manipulandum alleviates the already complex analysis of human-human physical interaction, for motor learning purposes a manipulandum with at least two degrees of freedom and larger workspace is desirable. Ganesh et al. [10] and Braun et al. [16] both used two identical planar robotic devices: two PFM planar robotic manipulanda [7] and two vBOT manipulanda [4], respectively. While any dual robotic setup can be made by linking two (preferably identical) existing robotic manipulanda, most of the devices as mentioned earlier are built in-house and are not commercially available. On the other hand, off-the-shelf solutions usually do not fit budgetary constraints or desired specifications.

We developed the Bipartner RObotic Setup (BROS), which is a setup consisting of two identical robotic manipulanda designed explicitly for studying physical human-human interaction during sensorimotor tasks. Our goal was to develop a setup consisting of two compact planar robotic manipulanda with a highly configurable control and software architecture and low isotropic endpoint mass. Besides describing the design and implementation process of the robot, we emphasize the usefulness of admittance control for human motor control research. Most manipulanda use impedance control, sometimes with feedforward control for passive dynamics compensation [6, 9] which heavily depend on the accuracy of the estimated device dynamics. We evaluate the performance of the robot in terms of admittance control capabilities with a focus on its efficacy for human-robot interaction and motor control studies.

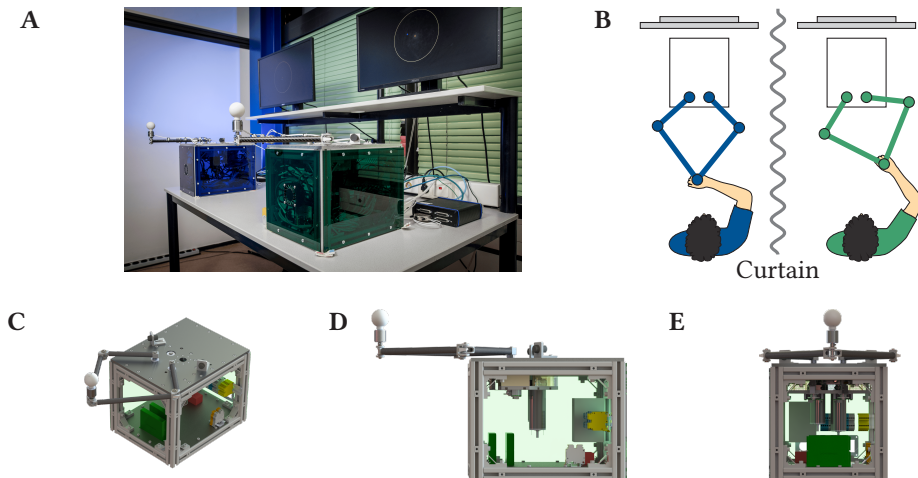


**Figure 2.1.** | Overview of BROS. (a) Overview photo of the BROS with the two robotic manipulanda and displays. (b) Schematic top view of the setup. (c–e) Isometric, side and front view renderings of the planar robotic manipulandum. The major mechanical and electronic components are built into the base of each manipulandum.

This paper first describes the robotic setup, design and implementation process, followed by the evaluation of the setup and its manipulanda. Lastly, we will assess its capabilities for performing physical human-human interaction experiments.

## 2.2. Design & Implementation

In this section, we first show an overview of the BROS, followed by a description of the design and implementation steps of the BROS. Because the main components are the two identical manipulanda, we will describe the design and evaluation for one robotic device, unless stated otherwise.

### 2.2.1. Overview

Figure 2.1 shows an overview of the BROS robotic setup and manipulandum. It comprises two identical planar parallel robotic manipulanda. Users hold the robot by the handle at the endpoint of the manipulandum, which is attached to the robot through a 6 DOF force/torque sensor. During experiments, a curtain is closed to isolate the participants so that they can only see their display and to minimize non-physical interaction.

## 2.2.2. Design requirements

The manipulanda of BROS are designed for the following requirements:

1. low endpoint mass such that the passive robot dynamics impede the user's arm movements as little as possible,
2. high structural rigidity such that high stiffness can be rendered,
3. a minimum elliptical workspace with a bounding box of  $350 \times 200$  mm based on the typical movement magnitude in motor control work (e.g. [17]),
4. a global conditioning index (GCI) (the condition number  $\kappa$  integrated over the usable workspace) larger than 0.7 for good manipulability [18],
5. the apparent dynamics at the endpoint by the user should be isotropic across the workspace such that changing device dynamics do not influence the user's motor control and
6. the robot should be able to deliver 25 N at the endpoint across the workspace continuously and maximally 75 N at the nominal position, similar to [6].

## 2.2.3. Topology, kinematics and dynamics

The BROS planar robotic manipulanda are parallel robots using a 5R symmetric parallel robot topology (see Fig. 2.2). We chose this robot topology mainly for the high structural rigidity, needed to render high stiffness, in combination with low endpoint mass, necessary for rendering low impedance, and positioning and measurement accuracy [19]. A disadvantage of such a parallel kinematic chain is the increased computational complexity of kinematics and in particular dynamics [20]. Here we describe the kinematics and a simplified model of the device dynamics which we used for design optimization and device control. The actuators and position sensors are situated at joints 1 and 5 (the 'shoulder' joints, indicated by  $P_1$  and  $P_5$ ) and are fixed to the base frame; the endpoint is located at joint  $P_3$ . Joints  $P_2$  and  $P_4$  are referred to as the 'elbow' joints. The links indicated by  $L_f$  and  $L_u$  are referred to as the 'forearm' links and 'upper arm' links, respectively. The origin of the Cartesian coordinate system is at the midpoint of the base segment  $L_b$ .

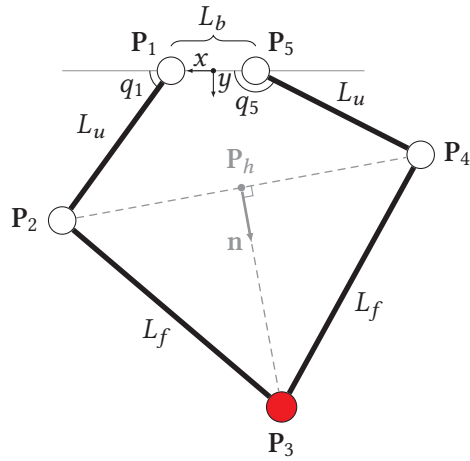


**Figure 2.2.** | Parallel 5R topology of the robotic device. The endpoint is at joint  $P_3$  and is indicated in red.

### Direct kinematics

The Cartesian endpoint position  $\mathbf{x} = [x_3, y_3]^T$  is directly related to the joint angles  $\mathbf{q} = [q_1, q_5]^T$ . The direct kinematics  $\mathbf{x} = f(\mathbf{q})$  are derived using the approach as described in Klein et al. [9]. The positions of joints  $P_1, P_2, P_4, P_5$  are:

$$\begin{aligned}\mathbf{P}_1 &= \left[ \frac{L_b}{2} \quad 0 \right]^T, \\ \mathbf{P}_5 &= \left[ \frac{-L_b}{2} \quad 0 \right]^T, \\ \mathbf{P}_2 &= [L_u \cos q_1 \quad L_u \sin q_1]^T + \mathbf{P}_1 \text{ and} \\ \mathbf{P}_4 &= [L_u \cos q_5 \quad L_u \sin q_5]^T + \mathbf{P}_5.\end{aligned}\tag{2.1}$$

Because both forearm links have length  $L_f$ , the triangle  $P_2P_3P_4$  is an isosceles triangle and therefore the projection of  $P_3$  should always be above the midpoint between  $P_2$  and  $P_4$ . By defining point  $P_h$  that is midway of points  $P_2$  and  $P_4$ , we can calculate the distance  $\|\mathbf{P}_h - \mathbf{P}_3\|$  and corresponding normal vector  $\mathbf{n}$  pointing from the midpoint  $P_h$  to  $P_3$ :

$$\begin{aligned}\mathbf{P}_h &= \frac{1}{2} (\mathbf{P}_2 + \mathbf{P}_4), \\ \mathbf{u} &= \mathbf{P}_4 - \mathbf{P}_2 = \begin{bmatrix} u_x \\ u_y \end{bmatrix} \text{ and} \\ \mathbf{n} &= \frac{1}{\|\mathbf{u}\|} \begin{bmatrix} u_y \\ -u_x \end{bmatrix}.\end{aligned}\tag{2.2}$$

Because of the isosceles right triangle formed by  $P_2P_hP_3$  we know the distance from  $P_h$  to  $P_3$  to be  $\sqrt{L_f^2 - \frac{1}{4} \|u\|^2}$ , such that the position  $P_3$  can be determined:

$$P_3 = P_h + n \sqrt{L_f^2 - \frac{1}{4} \|u\|^2}. \quad (2.3)$$

Because we are interested in the position of the endpoint  $P_3$  only, we denote the position of  $P_3$  as  $x$  from here on.

The geometric Jacobian  $J(q) = \partial x / \partial q$  relating endpoint velocity to the joint velocity ( $\dot{x} = J(q)\dot{q}$ ) can be calculated analytically from 2.3. The Jacobian can be used to calculate the conditioning number  $\kappa$  [19]:

$$\kappa = \frac{1}{\|J^{-1}\| \|J\|}, \quad (2.4)$$

where a value of 0 and 1 indicate minimum and maximum dexterity (i.e. isotropy) respectively.

## Dynamics

We derived a simplified model of the robot dynamics to optimize the design of the robot in terms of minimal passive device dynamics and for controller tuning. The joint-space dynamics of the robotic device can be written in the standard form

$$M(q)\ddot{q} + C(q, \dot{q})\dot{q} + D_c \text{sign}(\dot{q}) + D_v \dot{q} = \tau_q - J^T(q)F_e. \quad (2.5)$$

where  $M(q)$  is the mass matrix,  $C(q, \dot{q})$  includes the Coriolis and centripetal contributions,  $D_c$  and  $D_v$  are the Coulomb and viscous friction coefficients,  $\tau_q$  are actuator torques and  $F_e$  is an externally applied force at the endpoint [21].

Due to the coupling of the forearm links in the closed-loop kinematic chain, deriving the analytical solution of the device dynamics is complicated [19, 20]. Therefore, following the approach of Codourey [20], we used a simplified model which ignores the rotational inertia of the forearm links. To account for the mass of the left and right forearm links, we divided the mass  $m_f$  of each forearm link to the endpoint and corresponding elbow joints:  $\frac{1}{3}m_f$  is added to the endpoint mass  $m_e$  at  $P_3$  and  $\frac{2}{3}m_f$  is added to each elbow joint mass  $m_{el}$  at  $P_2$  and  $P_4$ :

$$m'_e = m_e + \frac{1}{3}m_f \text{ and } m'_{el} = m_{el} + \frac{2}{3}m_f. \quad (2.6)$$

Due to these simplifications, the mass matrix now consists of two main components: (1) the rotational inertia  $\Upsilon_q$  of both shoulder joints, upper arm links and elbow joints and (2) the point-mass  $m'_e$  of the endpoint. The rotational inertia matrix  $\Upsilon_q$  is

$$\begin{aligned}\Upsilon_q &= \begin{bmatrix} \Upsilon_{q,1} & 0 \\ 0 & \Upsilon_{q,5} \end{bmatrix} \text{ with} \\ \Upsilon_{q,i} &= \Upsilon_m k_r^2 + \Upsilon_s + L_u^2 \left( \frac{1}{3} m_u + m'_{el} \right), \quad i = 1, 5,\end{aligned}\tag{2.7}$$

where  $\Upsilon_m$  is the actuator rotor inertia,  $k_r$  the transmission ratio,  $\Upsilon_s$  the shoulder joint rotational inertia and  $m_u$  the upper arm link mass.

Contributions of the endpoint mass to the joint-space inertia and Coriolis and centrifugal terms are found by realizing that

$$\ddot{\mathbf{x}} = \mathbf{J}\ddot{\mathbf{q}} + \dot{\mathbf{J}}\dot{\mathbf{q}}.\tag{2.8}$$

Combining equations 2.5 to 2.8, the simplified dynamics are

$$\begin{aligned}\Upsilon_q \ddot{\mathbf{q}} + m'_e \mathbf{J}^T \mathbf{J} \ddot{\mathbf{q}} + m'_e \mathbf{J}^T \dot{\mathbf{J}} \dot{\mathbf{q}} + \mathbf{D}_c \text{sign}(\dot{\mathbf{q}}) + \mathbf{D}_v \dot{\mathbf{q}} = \\ \tau_q - \mathbf{J}^T \mathbf{F}_e.\end{aligned}\tag{2.9}$$

## 2.2.4. Mechatronic design and implementation

Figure 2.3 shows an overview of the mechatronic implementation of one manipulandum.

### Robot design

The link lengths  $L_b$ ,  $L_u$  and  $L_f$  are the main design parameters, as they greatly determine workspace, manipulability and dynamics.

Due to the force requirements specified in Section 2.2.2 and because we used DC motors which can generate relatively low nominal torque output, a transmission was needed. We used a capstan wire transmission with transmission ratio  $k_r$  for two reasons, (1) a capstan wire transmission is highly back-drivable and (2) it has no backlash compared to a geared transmission. However, it does have a lower stiffness than gear-based transmissions.

The link lengths and transmission ratio are the results of an optimization of a cost function which included the requirements described above using a genetic algorithm in MATLAB (see the results in Table 2.1). The resulting link lengths and transmission ratio led to a robot design with an elliptical workspace with a

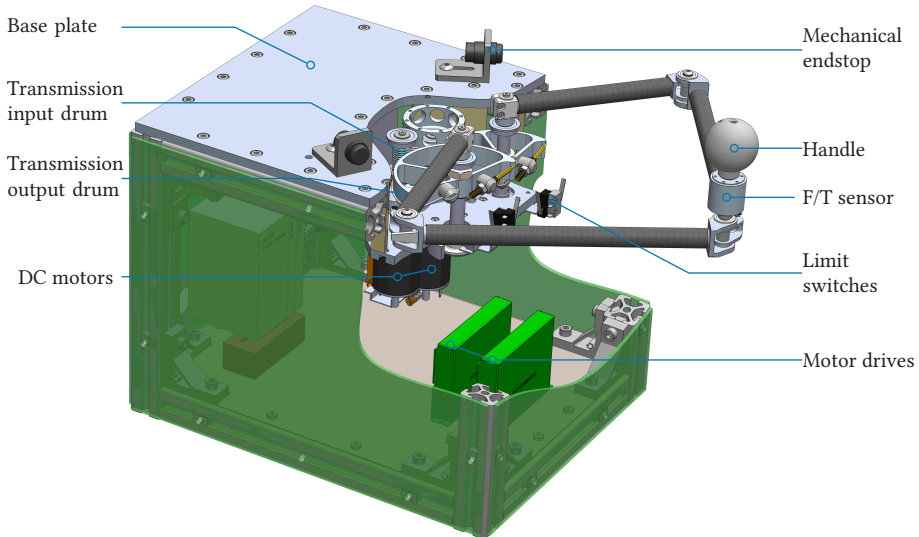


**Figure 2.3.** | Overview of the mechatronic implementation of one manipulandum.

bounding box of 355 by 215 mm, an average mass at the endpoint (averaged over the workspace) of 0.27 kg, maximum mass at the end of 0.55 kg at the usable workspace boundary and a global conditioning index of 0.74.

The condition number across the reachable workspace is given in Fig. 2.4A. Note that the usable workspace, indicated by the ellipse, is smaller than the total reachable workspace. We intentionally keep the robot's endpoint in the smaller usable workspace to avoid robot configurations with poor conditioning. The robot's nominal position – where the condition number is closest to 1 – is at  $\mathbf{x}_{\text{nom}} = [0, 0.245]^T$  m.

The maximum translational mass at the endpoint over the reachable workspace (including all inertia contributions) is calculated by finding the largest eigenvalue of the mass matrix expressed in operational space at the endpoint (denoted as  $\mathbf{M}_x$ ). We map the joint space mass matrix ( $\mathbf{M}_q = \Upsilon_q + m'_e \mathbf{J}^T \mathbf{J}$ ) to the endpoint operational space as follows [21]:

$$\mathbf{M}_x = \mathbf{J}^{-T} \mathbf{M}_q \mathbf{J}^{-1} = \mathbf{J}^{-T} \Upsilon_q \mathbf{J}^{-1} + m'_e \mathbf{I}^{2 \times 2}. \quad (2.10)$$

The mass of each component was estimated from CAD data, and the handle and force sensor were weighed.

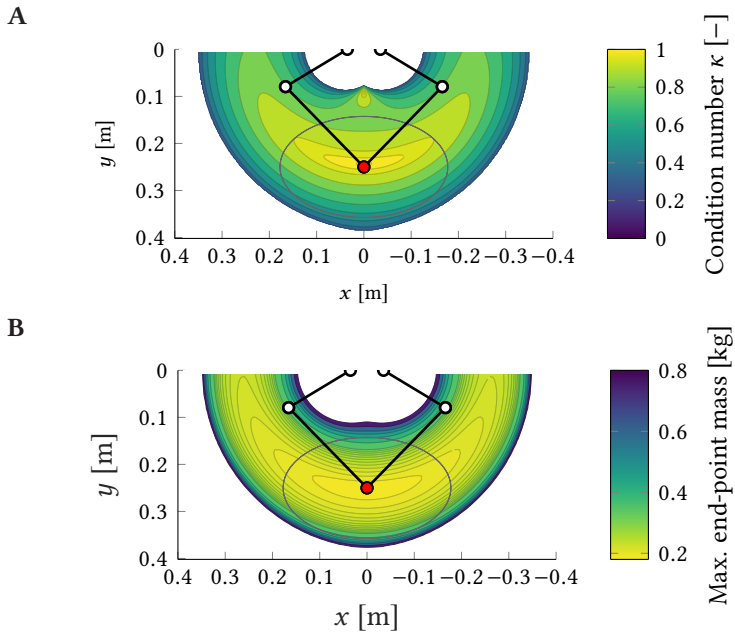


**Figure 2.4.** | Condition number and theoretical maximum endpoint mass, calculated using equation 2.10 across the workspace. **A** Theoretical condition number. **B** Theoretical maximum mass at the endpoint. Both figures show the robot configuration at the nominal position as well as the usable workspace.

## Mechanical design

All links consist of circular carbon-fiber reinforced tubes with an outer diameter of 15 mm and 1 mm wall thickness (mass density of  $65 \text{ g m}^{-3}$  and a modulus of elasticity  $E = 65 \text{ GPa}$ ). At the most extended position of the robot with the arms clamped, we expect a structural deflection of the links of 0.2 mm at the endpoint when applying a force of 75 N at the endpoint.

**Table 2.1.** | Robotic device design parameters and values.

Parameter	Value	[ $\text{m}$ ]
$L_b$	0.07	[ $\text{m}$ ]
$L_u$	0.238	[ $\text{m}$ ]
$L_f$	0.153	[ $\text{m}$ ]
$k_r$	7.3	[ $-$ ]

Other parts, including joints and transmission, are machined from aluminum. We used low-friction ball-bearings (SKF) for all joints. The planar manipulandum is housed in a rigid support frame made out of extruded aluminum profiles (MISUMI). The housing contains most of the electronics (motor drive, sensors and other circuitry) and is closed using transparent covers (see Fig. 2.1).

The handle at the endpoint is a 3D-printed sphere that is comfortable to hold. The handle is connected to the 6 DOF force/torque sensor at the robot's endpoint and can freely rotate around the out-of-plane axis.

### Actuation and sensors

The actuators at the shoulder joints are two Faulhaber 3890 Ho48CR brushed DC motors with a nominal torque of 0.24 N m and a stall torque of 2.9 N m. These motors have low rotor inertia ( $1.71 \cdot 10^{-9}$  kg m<sup>2</sup>) and no cogging due to them being coreless. The motors are connected to the transmission input shaft. Each motor is controlled by a Technosoft iPOS4808 BX-CAT motion controller in current control mode, which has a maximum continuous output current of 8 A, a peak output current of 20 A for a maximum of 2.5 s and a maximum nominal supply voltage of 48 V. Each motor drive has an EtherCAT controller and allows for multiple sensor read-outs directly onto the EtherCAT bus; in our case an incremental and an absolute encoder.

Position sensing is performed at each motor and each transmission output shaft. Each DC motor is equipped with an incremental encoder (Faulhaber IE3-1024L quadrature encoder, 1024 lines per revolution, 4096 counts in quadrature mode). An absolute encoder (MU1C, iCHaus) with a 16-bit per revolution resolution is connected to each transmission output shaft. Using these position sensors, we expect a worst-case measurement inaccuracy of  $dx \approx 26$  m at the extreme of the workspace [19]. Joint velocity is calculated using a discrete-time differentiation of the position signals, followed by a second-order Butterworth low-pass filter with a 70 Hz cut-off frequency. The translational position and velocity of the endpoint are calculated using the direct kinematics and jacobian (see equations 2.1 to 2.3).

Forces and torques exerted onto the endpoint by the user are measured using a high-precision 6 DOF force/torque sensor (ME Meßsysteme K6D27 sensor with a custom 100 N and 2 N m range). The sensor's GSV-8DS EC amplifier (ME Meßsysteme) has 24-bit ADCs and an EtherCAT controller so that it can directly connect to the EtherCAT chain. We measured force sensor drift and measurement variance for 80 min. The force sensor measurement variances for the sensor's local  $x$ - and  $y$ -axes are similar and are in the range of  $1.85 \cdot 10^{-5}$  N<sup>2</sup> to  $1.93 \cdot 10^{-5}$  N<sup>2</sup>. The drift of the  $x$  axis of the sensor was approximately 19.8 mN h<sup>-1</sup> (first-order linear regression).

## **Software implementation**

The robots are controlled using the EtherCAT real-time control system (EtherCAT Technology Group), which is controlled through TwinCAT 3 (Beckhoff). The advantages of using the EtherCAT control system include low loop delay and jitter (< 100 ns) and simple reconfiguration of additional sensor slaves. Furthermore, any PC can serve as the EtherCAT master device. Physical processing cores can be isolated to be solely utilized for the EtherCAT real-time system execution, eliminating operating system-related timing delays. TwinCAT is capable of using compiled MATLAB Simulink (Mathworks) models for real-time control. Communication between the TwinCAT real-time kernel and the Windows operating system is performed using the TwinCAT Automation Device Specification (ADS) router.

The experiment control software, which handles the communication with the real-time EtherCAT system, is implemented in C<sup>++</sup> on the same system. Experiment visualization is done using OpenFrameworks (version 0.10.0) which handles the low-level OpenGL programming for minimal latency and hardware-accelerated display of movements. Data for graphics visualization is polled from the real-time system and updated at 120 Hz. Complete experiment protocols can be programmed intuitively by human-readable XML files.

## **Safety**

Multiple safety features are implemented: mechanical endstops, limit switches, emergency buttons, software limits and watchdog timers. To complement the mechanical endstops for each upper arm (see Fig. 2.1C), we implemented two limit switches per actuator at the extremes of their predefined range of motion. When pressed, the limit switches pull the enable circuits of both drives down, disabling both drives. Furthermore, each robotic device has an emergency button: when pressed, all motor drives of both robotic devices are disabled. We also implemented software limits for position, velocity and maximum force. When any of these parameters exceeds a threshold, all motor drives are disabled. Lastly, all EtherCAT slaves (the motor drives and the Beckhoff EtherCAT terminals) have built-in watchdog timers. These watchdog timers monitor the communication between the slave and the master computer. In case of a communication interruption (unplugging of a data cable or master computer crash), the watchdog timer in the motor drives will disable the drives after 50 ms. As a second layer of safety, the motor drive enable circuit is powered using a Beckhoff EL2008 digital out terminal which also includes a watchdog timer set to 50 ms. Once triggered, this watchdog timer will pull the digital output down, disabling the motor drive

enable circuit and disabling the motor drives.

The electrical safety and electromagnetic compatibility are ensured by using a REOMED 2200 W medical isolator (REO) and redundant earthing. Where possible, shielded and screened electrical cabling is used. The covers of the support structure prohibit the user from touching any internal parts.

### 2.2.5. Manipulandum admittance controller

We chose an admittance control strategy for how a manipulandum reacts to the user's force input on the handle. In admittance control, the opposite of impedance control, the force exerted by the user onto the handle is measured and used to calculate a setpoint – through a model of desired virtual dynamics – for a lower-level position controller [22]. Figure 2.5 shows the basic control diagram of admittance control. The human exerts a force  $F_h$  onto the robot, which is used as an input to a virtual model  $Y_m$ . This virtual model, for example, a mass-damper dynamic system, outputs a desired position  $x_d$  setpoint for the low-level controller  $C_p$ . The controller  $C_p$  attempts to enforce  $x_d$  onto the robot  $Y_r$  using a controller force  $F_c$ , resulting in the robot's motion  $x$ .

For our application, admittance control has some advantages over impedance control which is often used in other devices (e.g. [4, 9]). Because the chosen robot configuration results in changing dynamics and conditioning across the workspace – for instance, the mass at the endpoint varies considerably over the workspace – admittance control allows us to make them isotropic. Although this can be achieved with impedance control, for instance by using feedforward dynamic compensation of the passive device dynamics, this heavily relies on how well the device dynamics can be estimated. Furthermore, for admittance control, it is more straightforward to render any dynamics, such as stiff objects and objects with high mass, which is more difficult in impedance control. For instance, when rendering a virtual wall in admittance, you only need to limit the desired position  $x_d$  to not cross the wall.

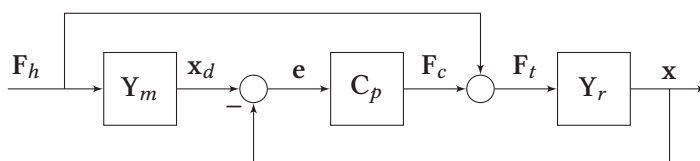


**Figure 2.5.** | Admittance control diagram for one manipulandum.

The apparent admittance  $Y_a(s)$  of the admittance controller shown in Fig. 2.5 is calculated by deriving the closed-loop transfer function from input  $F_h$  to  $x$ :

$$Y_a(s) = \begin{bmatrix} \frac{x(s)}{F_{h,x}(s)} & 0 \\ 0 & \frac{y(s)}{F_{h,y}(s)} \end{bmatrix} = (I^{2 \times 2} + Y_r(s)C_p(s))^{-1} (Y_r(s) + Y_r(s)C_p(s)Y_m(s)). \quad (2.11)$$

The apparent admittance indicates the admittance the user feels during the interaction, taking the controller and robot dynamics into account. In the limit for high control gains, the apparent admittance converges to the desired admittance.

We set the virtual model dynamics of each robotic device to a mass ( $m_v = 0.3 \text{ kg}$ ) and damper ( $b_v = 0.2 \text{ N s m}^{-1}$ ) system. Although lower inertia is possible (e.g., the maximum mass of approximately 60 % of the usable workspace is smaller than 0.3 kg), these settings provide a good trade-off between apparent device dynamics and stability across dynamic conditions, such as rendering a rigid connection between the two robots' endpoints.

The low-level position control loop was closed using a PD controller ( $C_p$ ) in operational space [21]. The PD controller gains were tuned such that the endpoint position tracking behavior was stable across the usable workspace. The position gain  $k_p$  and differential gain  $k_d$  of controller  $C_p$  are set to  $1500 \text{ N m}^{-1}$  and  $18 \text{ N s m}^{-1}$ , respectively. The controller gains are limited mainly due to mechanical constraints and the added phase lag in the closed loop due to velocity estimation, which we will analyze and discuss further in the next sections.

## 2.2.6. Teleoperation controller

A set of two coupled manipulanda is in principle a typical teleoperation setup. The two robotic devices can be coupled by interchanging the virtual spring force connecting both robots and adding the spring force to the virtual model force input. Figure 2.6 shows the control scheme of such a coupling: the difference in the desired robot position results in a spring force  $F_s$ , which is added to the virtual model inputs. Admittance control allows for stable coupling of two robot devices compared to impedance control alternatives; the measured force can be interchanged directly as if both partners are applying force onto a common virtual model [23]. The low-level position control loop stiffness then limits the maximum render stiffness.

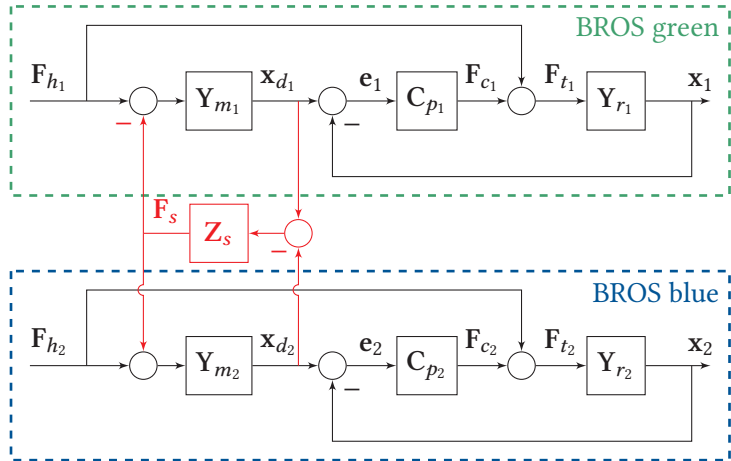


**Figure 2.6.** | Teleoperation controller diagram for two coupled manipulanda. The two coupled manipulanda are denoted by BROS green and BROS blue.  $Z_s$  denotes the connection dynamics coupling the two manipulanda, for instance a linear spring.

## 2.3. Evaluation

We performed some tests to evaluate the robotic device's performance. First, we tested the robot's low-level position control loop by measuring the robot's ability to render (closed-loop) stiffness and by its closed-loop position tracking bandwidth. Second, we evaluated the admittance control performance. Lastly, we evaluated the usability of the BROS for studying human-human interaction. We summarized the performance of a manipulandum in Table 2.2.

### 2.3.1. Closed-loop stiffness rendering and force production

The closed-loop stiffness at the handle was estimated at the nominal position in eight directions. We simulated nine springs in the virtual model, with the desired stiffness ranging from  $20 \text{ N m}^{-1}$  to  $400 \text{ N m}^{-1}$ . Per spring, we manually pulled the endpoint handle from the nominal position in eight directions. The measured force, handle position (as measured by the encoders) and handle velocity were recorded. We regressed a mass-spring-damper system in two dimensions to the measured data. The resulting stiffness in  $x$  and  $y$  was compared to the desired stiffness, see Fig. 2.7. Due to the high similarity in measured stiffness in  $x$  and  $y$ , we combined these stiffnesses in  $x$ - and  $y$ -direction in Fig. 2.7. When the desired stiffness of  $200 \text{ N m}$  is simulated, we measured a stiffness of  $175 \text{ N m}$ . The lower actual stiffness is due to the low-level position loop stiffness, which acts as a series compliance element with the desired stiffness ( $(1/1500 + 1/200)^{-1} =$

**Table 2.2.** | Performance measures of one manipulandum

Performance measure	Value
Usable workspace (ellipse with a bounding box of $L \times W$ )	0.355 m $\times$ 0.215 m
Global conditioning index	0.74 –
Position resolution <sup>□</sup>	26 m
Velocity resolution <sup>□, ▽</sup>	26 mm s <sup>-1</sup>
Max. velocity (manual excitation)	1.05 m s <sup>-1</sup>
Max. acceleration (closed-loop pos. input)	108.4 m s <sup>-2</sup>
Max. acceleration (manual excitation)	16.7 m s <sup>-2</sup>
Force/torque sensor range (in $x$ and $y$ )	100 N; 2 N m
Force sensor resolution (in $x$ and $y$ )	30 N
Max. force production	50 N
Max. passive endpoint mass <sup>□</sup>	0.55 kg
Closed-loop position bandwidth (in $x$ and $y$ )	21 Hz
Admittance control bandwidth	6.5 Hz
Control frequency	1 kHz

□: The handle was at the position with lowest condition number (furthest away from the robot)

▽: Velocity resolution is calculated by dividing the position resolution by the sampling time (0.001 s)

175 N m<sup>-1</sup>), see Fig. 2.7). This means that we need to compensate for the inner loop position control stiffness when setting the desired stiffness. Note that we did not take the structural stiffness of the device into account.

Each parallel manipulator of BROS is capable of generating over 50 N of force at the endpoint. We tested this by slowly increasing the generated force at the endpoint by open-loop control in eight directions. The user firmly held the handle at the endpoint. The force/torque sensor measured the force exerted by the robot onto the handle. We did not test forces over 50 N for safety reasons, because we do not expect to use such high forces during the intended human-human interaction experiments.

### 2.3.2. Closed-loop position bandwidth performance

The control bandwidth of the robot was assessed by analyzing the closed-loop position-position tracking performance at the endpoint *at the nominal position*. We used sum-of-sines excitation signals for the desired endpoint position  $\mathbf{x}_d$  in operational space (see Chapter A for more information). The tracking performance was measured over five repetitions of 30 s with a sampling frequency of

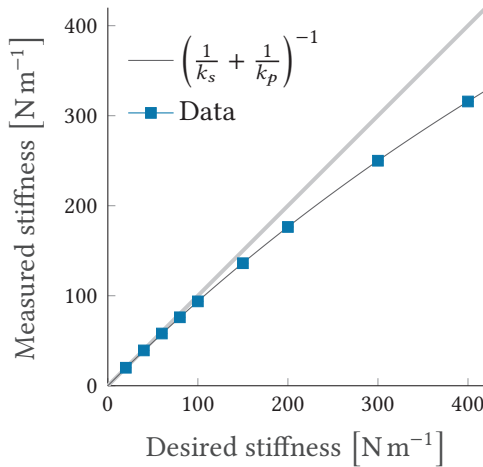


**Figure 2.7.** | Comparison of desired stiffness and measured stiffness. We evaluated several desired stiffness levels. The expected measured stiffness, based on the closed-loop position controller in series, is given as well. We measured the stiffness at each desired stiffness level five times, while moving the handle in eight directions. The markers indicate the mean measured stiffness, where the measured stiffness in  $x$  and  $y$  are combined. Although not visible, the small error bars (standard error of the mean) indicate that the measurements are highly repeatable.

1 kHz. The resulting robot endpoint position  $\mathbf{x}$  was recorded. The measured frequency response  $H_{\mathbf{x}_d, \mathbf{x}}$  for both the  $x$  and  $y$  axes are shown in Fig. 2.8. Our main observations are: (1) the frequency responses for both axes are very similar and show high consistency across repetitions, (2) the gain is approximately one up to 10 Hz for both axes, well above the expected human hand movement bandwidth, (3) a resonant peak occurs at approximately 17 Hz and (4) the frequency response crosses the  $-3 \text{ dB} (\sqrt{0.5})$  point at 21 Hz. Increasing the differential action of the low-level position loop PD controller should decrease the resonance peak; however, we were not able to increase damping and position gain further during tuning, most likely due to the second-order filter used for the velocity calculation and mechanical transmission resonance.

The sharp increase in the frequency response magnitude near 100 Hz in Fig. 2.8 is likely due to a mechanical resonance of the capstan transmission. To further analyze the capstan transmission dynamics, we clamped one of the upper arm links to the base of the robot (hence fixing the transmission output shaft) and sent a sum-of-sines torque excitation signal to the motor. We measured the angular motor position using the motor encoders, the (clamped) output shaft angular position using the absolute encoders and commanded and actual motor torque. The measured frequency response  $H_{\tau_c, q_m}(j\omega)$  of the commanded torque  $\tau_c$  to

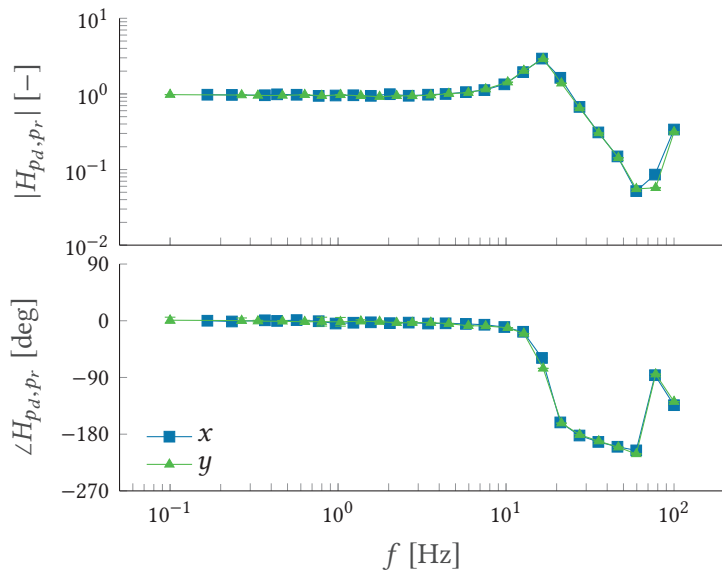


**Figure 2.8.** | Closed-loop position tracking frequency responses of the  $x$  and  $y$  directions at the nominal position. Markers and error bars indicate the mean and standard error of the mean, respectively. Note that the error bars are small and practically not visible, indicating that the frequency response results across the five repetitions was highly repeatable.

motor position  $q_m$  (see Fig. 2.9) indeed reveals a transmission resonance peak at  $f_d \approx 110$  Hz. This low-frequency resonance most likely occurs due to the compliance in the cable transmission [24] and reduces stability margin, subsequently forcing controller gains down [25]. We will discuss options for curing the low-frequency resonance peak and its effect on stability limits in the discussion.

### 2.3.3. Admittance controller performance

We analyzed the performance of how well a robotic device can render the desired admittance using two metrics. First, we tested the isotropy of the rendered apparent admittance across the workspace and compared it to the passive device dynamics. Second, we analyzed the bandwidth over which the robotic device can render the desired admittance.

#### Isotropic apparent admittance

To compare the measured apparent dynamics and passive dynamics, we estimated the apparent endpoint mass and passive device endpoint mass to assess whether the admittance control approach indeed leads to isotropic dynamics

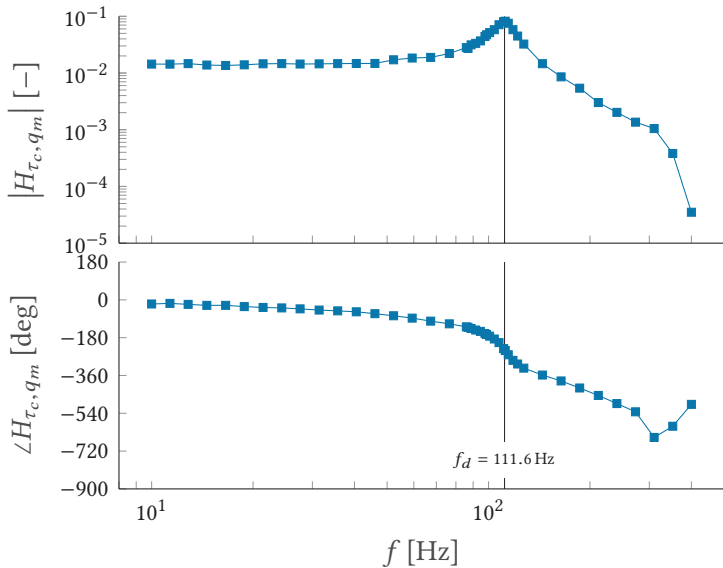


**Figure 2.9.** | Frequency response of the capstan transmission dynamics. The torque excitation signal consisted of 42 non-harmonic sines, equally spread over a bandwidth of 10 Hz to 400 Hz. Note that we decreased the frequency spacing between 90 Hz to 130 Hz to properly capture the resonance peak. The maximum absolute requested torque of the excitation signal was scaled to 0.2 N m.

across the workspace. To estimate the apparent admittance and passive device dynamics, we manually moved the handle at nine locations in all directions with different velocities and accelerations while staying close to the initial location for 60 s. This measurement was done twice: once when the admittance controller was switched on to measure the apparent mass and once when the device was switched off to measure the passive device mass. We recorded the force applied at the endpoint and the resulting robot movement and the endpoint position. Endpoint velocity and acceleration were obtained by time differentiation. To obtain the measured apparent mass, we fitted the desired dynamics  $\mathbf{Y}_m$  (a mass-damper system in  $x$ - and  $y$ -directions) to the measured data. The resulting apparent mass matrix per location is shown in Fig. 2.10 including the expected apparent mass (e.g.,  $m_v = 0.3$  kg). To obtain the passive endpoint mass, we fitted the dynamic model (equation 2.9) to the measured data. The passive endpoint mass was then calculated using equation 2.10. All model fits were performed using MATLAB’s `fmincon` algorithm and showed high  $R^2$  values ( $> 0.9$ ) indicating a good fit to the measurement data.

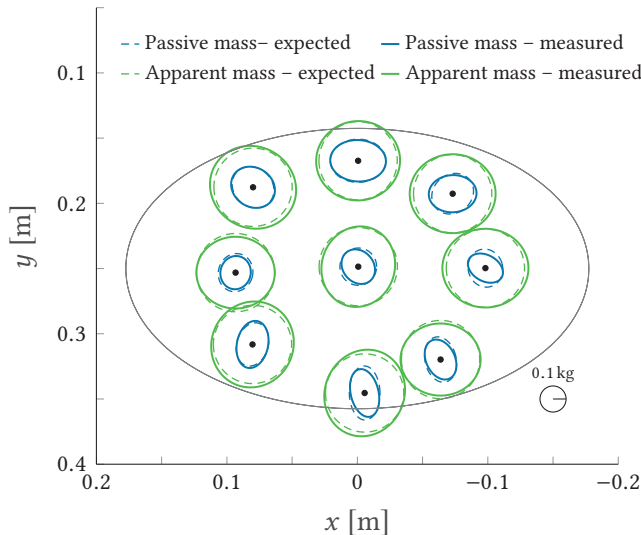


**Figure 2.10.** | Comparison of the expected versus measured passive and apparent mass across the workspace. The locations are the average positions of each measurement. The gray ellipse indicates the usable workspace. The admittance control approach leads to isotropic mass at different positions in the workspace.

Figure 2.10 compares the expected and measured apparent endpoint mass and expected and measured passive endpoint mass at the nine locations in the usable workspace. The apparent mass is mostly isotropic across the usable workspace compared to the passive endpoint mass. The advantage of the admittance control approach is evident for endpoint locations further away from the nominal position (i.e., locations with a smaller condition number). Dynamic feedforward compensation of the passive device dynamics could improve the passive device dynamics (e.g. [9]), however precisely identifying the passive device dynamics is not trivial. The admittance control approach ‘solves’ this problem for us. Small discrepancies are seen between the expected and measured endpoint masses; our manual excitation of the robot to measure these data is likely an important factor. Note that the desired apparent mass was set to 0.3 kg, which is higher than the maximum passive endpoint mass; this was done to ensure unconditional stability for all practical human-robot interaction scenarios expected during experiments.

## Apparent admittance bandwidth

The bandwidth over which the desired dynamics can be rendered is examined by comparing the desired virtual dynamics  $\mathbf{Y}_m$  with the apparent admittance inferred from  $\mathbf{Y}_m$ ,  $\mathbf{C}_p$  and  $\mathbf{Y}_r$ , denoted as  $\mathbf{Y}_a$ , and felt or measured apparent admittance  $\hat{\mathbf{Y}}_a$ , where

$$\begin{aligned}\mathbf{Y}_a(s) &= \begin{bmatrix} \frac{x(s)}{F_{h,x}(s)} & 0 \\ 0 & \frac{y(s)}{F_{h,y}(s)} \end{bmatrix} = \begin{bmatrix} Y_x(s) & 0 \\ 0 & Y_y(s) \end{bmatrix} \text{ and} \\ \hat{\mathbf{Y}}_a(s) &= \begin{bmatrix} \hat{Y}_x(s) & 0 \\ 0 & \hat{Y}_y(s) \end{bmatrix}.\end{aligned}\quad (2.12)$$

We define the bandwidth as the lowest frequency at which the ratios of magnitude of the measured apparent admittance and the desired apparent admittance ( $|\hat{\mathbf{Y}}_a|/|\mathbf{Y}_a|$ ) is smaller than 0.9 or larger than 0.9<sup>-1</sup>.

The frequency response of the desired virtual dynamics  $\mathbf{Y}_m$  is calculated with a mass of 0.3 kg and a damping of 0.2 N s m<sup>-1</sup>. We extracted the frequency response of the robot dynamics  $\mathbf{Y}_r$  (from commanded torques to resulting robot position in  $x$  and  $y$  directions) using the data from the position control loop bandwidth evaluation, which means we can only evaluate  $\mathbf{Y}_r$  at the frequencies given in Table A.1. The frequency response of the controller  $\mathbf{C}_p$  was also evaluated at these frequencies, using the tuned position controller values. The inferred apparent admittance is then calculated using equation 2.11. The measured apparent admittance  $\hat{\mathbf{Y}}_a$  was assessed by randomly applying forces onto the robot endpoint at different frequencies and in all directions for five repetitions of 120 s each at the nominal position. We took care to stay close to the nominal position while moving the endpoint. Note that the human user applying the forces was only able to provide frequencies in the range of approximately 0.2 Hz to 7.5 Hz.

Figure 2.11 shows the desired model dynamics  $\mathbf{Y}_m$ , the inferred apparent admittance  $\mathbf{Y}_a$  and measured apparent admittance  $\hat{\mathbf{Y}}_a$ . We see that the inferred and measured apparent admittance in both  $x$ - and  $y$ -directions match well. Furthermore, the inferred and measured apparent admittance results match the desired admittance at least up to 6 Hz. Above 6 Hz to 7.5 Hz the apparent admittance is still similar to the desired dynamics; however, the measured apparent admittance bandwidth already exceeds the bandwidth of typical human arm movements (for instance, the maximum frequency of human arm movements during tracking tasks is around 4 Hz [26]).

Because the apparent admittance is, among others, a function of the robot dynamics  $\mathbf{Y}_r$ , the apparent admittance bandwidth varies over the workspace. To analyze this variation, we simulated the apparent admittance using equation 2.11

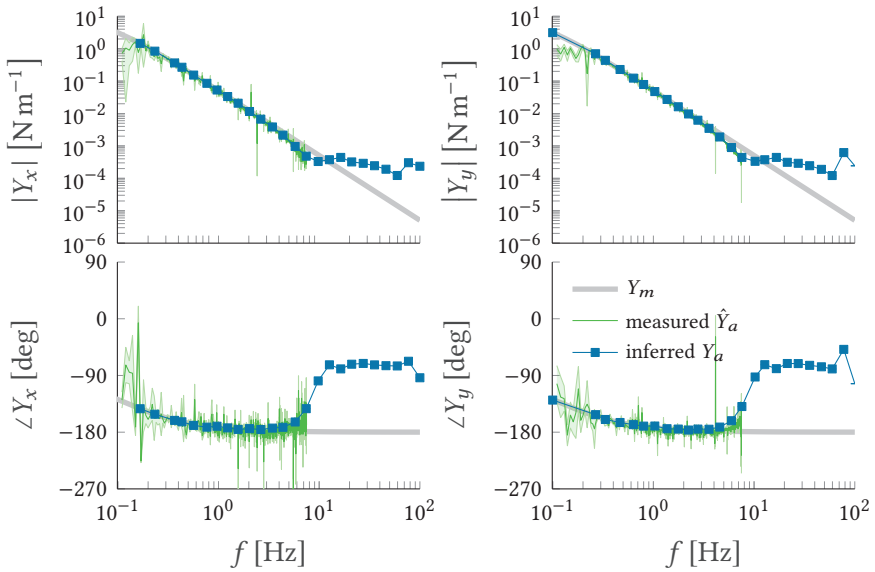


**Figure 2.11.** | Desired admittance versus inferred and measured apparent admittance. The left and right columns present the magnitude and phase of the desired, inferred and measured apparent admittance in the  $x$ - and  $y$ -directions at the nominal position, respectively. The measured apparent admittance shows the mean and standard error of the mean.

across the usable workspace. We estimated the parameters of the simplified dynamics (see equation 2.9) using a model fit as used for estimating the passive device dynamics as described above. The frequency response of the apparent admittance is then evaluated across the workspace and compared to the desired admittance. The apparent admittance bandwidth is defined as described above.

Figure 2.12 shows the simulated apparent admittance bandwidth across the usable workspace. The smallest bandwidth between the  $x$ - and  $y$ -directions was taken at each location. The further the endpoint is from the base of the robot, the lower the apparent dynamics bandwidth. The lowest bandwidth is approximately 4.8 Hz at the farthest position of the workspace, which is still above the expected bandwidth of human control and tracking behavior. Note that the simulated results are highly dependent on the estimated device dynamics parameters; as mentioned before, estimating the passive device dynamics yields results of varying quality. The bandwidth of the measured and inferred apparent admittance could be improved by improving the position control loop performance.

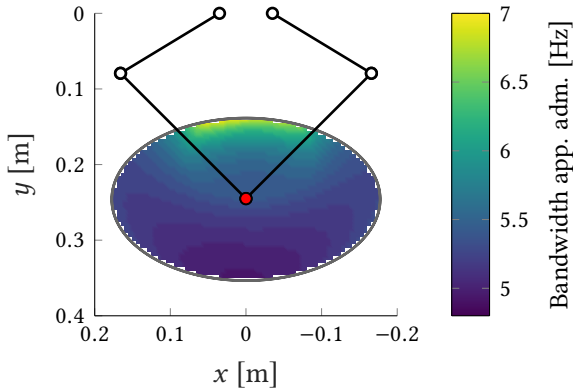


**Figure 2.12.** | Simulated bandwidth of the apparent admittance across the usable workspace. The shown bandwidth is the smallest frequency of the apparent admittance bandwidth in either the  $x$ - or  $y$ -direction.

### 2.3.4. Experimental evaluation

Here we present the results of an experiment to evaluate the performance of BROS for studying physical human-human interaction. This experiment also serves as a showcase of using an admittance control approach to teleoperation, in which the robots are coupled through a spring  $Z_s$  with different connection dynamics (see Fig. 2.6).

Ganesh et al. [10] showed that physical interaction through a compliant connection (a computer-generated spring) during a continuous tracking task leads to better tracking performance compared to performing the tracking task alone. More importantly, they found that you improve by interaction *regardless* of whether your partner is better or worse than you at the task. We performed a similar experiment to the one described by Ganesh et al. [10].

#### Experiment setup

We recruited 10 participants (aged  $24.5 \pm 2.2$  years, four females and six males), which performed the experiment in five pairs. All participants performed the same planar tracking task. The goal was to track a target with a cursor as accurately as possible on a display. The cursor was controlled by moving the robot's handle. Each participant had a manipulandum and display, see Fig. 2.1.

The target moved continuously during trials of 48 s. The data of the first 3 s were discarded to remove any transient tracking behavior at the start of the trial. The target movement was always the same for both partners. The target movement was defined as sum-of-sines:

$$\begin{aligned}
 x(t) = & 2.11 \sin(0.63t + 4.86) + 2.05 \sin(1.10t - 6.88) \\
 & + 1.91 \sin(1.73t + 0.18) + 1.72 \sin(2.67t - 8.49) \\
 & + 1.42 \sin(4.24t + 3.75) + 1.31 \sin(5.50t - 4.28) \\
 & + 1.13 \sin(6.75t - 9.35) + 0.99 \sin(8.01t - 0.54) \\
 y(t) = & 1.95 \sin(0.79t + 4.86) + 1.89 \sin(1.26t - 6.88) \\
 & + 1.77 \sin(2.04t + 0.18) + 1.59 \sin(2.98t - 8.49) \\
 & + 1.31 \sin(4.56t + 3.75) + 1.21 \sin(5.18t - 4.28) \\
 & + 1.05 \sin(6.44t - 9.35) + 0.91 \sin(7.70t - 0.55).
 \end{aligned} \tag{2.13}$$

The tracking signal required hand movements over a circular workspace with a diameter of 18 cm, an average velocity of 13.9 cm s<sup>-1</sup> and a maximum velocity of 28.9 cm s<sup>-1</sup>. Each pair performed 48 trials of the tracking task divided over six blocks.

Two types of trials were used in the experiment: *connected* and *single* trials. During some trials, the partners in a pair interacted with each other through a virtual spring; these trials are denoted as *connected* trials. The spring force allowed the partners to physically interact, while still being able to execute the tracking task independently. The computer-generated virtual spring (i.e., the connection dynamics  $Z_s$ , see Fig. 2.2.6) consisted of a spring stiffness of  $k_s = 120 \text{ N m}^{-1}$  (same stiffness as used by Ganesh et al. [10]) and damping  $b_s = 2.5 \text{ N s m}^{-1}$ :

$$F_s = k_s (\mathbf{p}_p - \mathbf{p}_o) + b_s (\mathbf{v}_p - \mathbf{v}_o), \tag{2.14}$$

where  $F_s$  is the spring force exerted on a participant's hand,  $\mathbf{p}_p$  and  $\mathbf{v}_p$  and  $\mathbf{p}_o$  and  $\mathbf{v}_o$  are the partner's and the participant's own position and velocity, respectively. The elastic force was exerted onto both partners' hands by the robotic manipulanda. If a partner moved away from the other partner, they both experienced a force pulling them toward each other.

The partners were not connected during the remaining *single* trials. The sequence of single (S) and connected (C) trials was {[SCCSCSCS] [SCCSCSCS] [CSCSCSCC] [SCSSCSCS] [CSCSCSCC] [SSCSCSSC]}. Participants were not explicitly made aware whether the trial was a single or connected trial.

Participants gave informed consent to participation in the study. The study was designed following the principles of the Declaration of Helsinki.

An expedited assessment of the study by the Medical Ethical Review Board of the University of Twente (METC Twente) showed that the study poses minimal risk and under Dutch law does not need full ethical review.

## Data analysis

We focus on the performance improvement due to physical interaction following the approach of Ganesh et al. [10] and Takagi et al. [11]. Motor performance was measured as the root-mean-square (RMS) of the tracking error, denoted by  $E$  (in cm), recorded at 1 kHz. We calculated performance for single trials ( $E_s$ ) and connected trials ( $E_c$ ). Since the compliant virtual springs still allowed independent tracking execution,  $E_c$  of each partner is not necessarily the same.

Similar to Ganesh et al. [10] and Takagi et al. [11], we examine the relationship between improvement due to the haptic interaction and the relative performance difference between partners. This allows us to study whether interaction with a better or worse partner results in differences in the benefits of the interaction for different skill levels. The improvement in performance due to interaction ( $I$ ) is calculated as

$$I = 1 - \frac{E_c}{E_s}, \quad (2.15)$$

where  $E_c$  is the performance in a connected trial and  $E_s$  is the performance in the single trial following the connected trial. The relative performance ( $R$ ) of the partner you interact with is calculated by

$$R = 1 - \frac{E_{s,p}}{E_s}, \quad (2.16)$$

where  $E_{s,p}$  is the partner's performance during the single trial and  $E_s$  is the participant's own performance during the same single trial. To highlight the trends in the data, we calculated the mean performance improvement in bins that are 5 % of relative performance  $R$  wide.

To analyze whether physical interaction leads to significant improvement compared to performing the task alone, we used Wilcoxon sign-rank tests (one-sample) per bin to test whether the improvement per bin had a median larger than zero at a level of significance of 0.05.

## Results

The improvement in task performance during a connected trial compared to both partners performing the task alone is plotted against the relative performance difference between the partners in Fig. 2.13.

Physical interaction generally leads to improvement in motor performance *during* interaction when connected to a better partner (top-right quadrant). We found significant improvement for all positive relative performance bins, i.e. when the relative partner performance is  $R > 5\%$  (all sign-rank tests resulted in  $p < 0.01$ ). Being connected to a worse partner did not significantly improve performance (top-left quadrant). All sign-rank tests for all bins  $R < 0$  did not reveal significant differences except for the bin spanning the relative range  $R = [-17.5, -12.5]\%$ .

Although our evaluation experiment showed similar results to previous work [10] on physical human-human interaction, we could not confirm their main conclusion that physical interaction leads to improvement regardless of partner performance. Although we used similar spring dynamics, we found no significant improvement when interacting with a worse partner. Note that we used a different, more difficult target tracking sum-of-sine signal compared to Ganesh et al. [10]; however, we did not introduce a visual perturbation to during the tracking task (a visuomotor rotation), as Ganesh

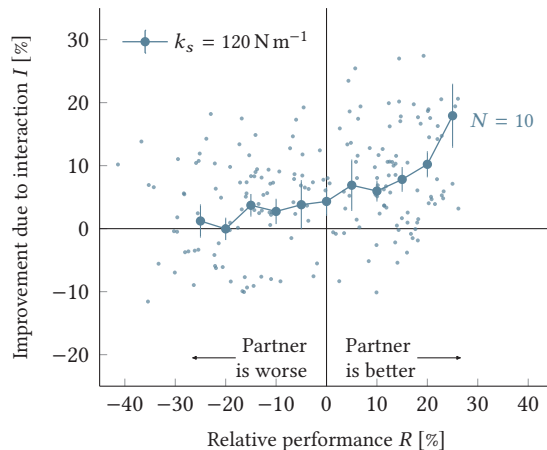


**Figure 2.13.** | Relative performance versus improvement due to physical interaction. The horizontal axis shows the relative performance  $R$  between interacting partners, the vertical axis shows the improvement  $I$  due to interaction: a positive improvement means that interaction helps. The error bars show the mean and standard error of the mean improvement per bin.

et al. [10] did. Nonetheless, the experiment demonstrated the capability of BROS to investigate physical human-human interaction.

## 2.4. Discussion

This paper described the design, implementation and evaluation of BROS, a robotic setup with two 2-DOF manipulanda designed for studying physical human-human interaction. We showed that the device can render the desired admittance across the workspace and can be used for studying human-human interaction. The compact design of the robotic manipulanda of BROS allows for multiple configurations of the setup (for instance two manipulanda for human-human interaction or bimanual motor control or one for unimanual motor control studies). Multiple safety features minimize the risk for the user.

### Manipulandum evaluation

The main design parameters for the robotic devices were a minimal passive mass at the end-point, high force production and good robot conditioning while providing a sufficiently large workspace. BROS' capabilities to render admittance dynamics isotropically across the workspace allow for a useful tool to study human-human interaction. We assessed the uniformity in the  $x$ - and  $y$ -directions of the admittance dynamics by evaluating the apparent mass at several points across the workspace. Furthermore, we showed that the bandwidth with which the manipulanda can render the desired dynamics exceeds the typical bandwidth of human arm movements in a plane (e.g. [26]). The apparent passive mass at the end-point is relatively low compared to other devices and permits the stable rendering of low mass dynamics compared to other (impedance-controlled) devices (e.g. [4, 9]). The maximum force production of BROS is lower than other similar devices [4, 6, 9]; however, its force production is sufficient for our experimental goals.

### Future hardware improvements

The evaluation test results suggest that some improvements can be made to improve BROS' performance. First, the position control loop performance can be improved in different ways. The velocity estimation is currently performed by using a discrete-time differentiation of the joint positions in combination with a second-order Butterworth filter with a cut-off frequency at 70 Hz. Other methods such as the first-order adaptive windowing (FOAW)

[27] or implementing a Kalman filter could yield better results. We could also use gyroscopes to measure the rotational rate of the joints directly. The position control loop can be further improved by implementing inverse dynamic control [21]. However, due to the uncertainty in the identified dynamic model parameters, such as identified static and viscous friction, we did not find significantly better performance using inverse dynamics compared to the (much simpler) PD controller we implemented instead; still, further research is warranted. Second, the low-frequency resonance mode originating in the capstan transmission reduces control stability margins. Acceleration feedback, for instance through inertial measurement units can help to cure low-frequency resonance [25]. At the moment we implemented a single PD controller; however, we could implement more complex control strategies, such as gain scheduling. Furthermore, the resonance frequency of the capstan transmission could be shifted to higher frequencies and thus reducing its impact by increasing the transmission stiffness, for instance by increasing the cable pretension or using cables with larger diameters [24].

In summary, the BROS provides a useful and versatile tool to study physical human-human interaction, bimanual motor control and upper-extremity impairment assessment [28, 29], other applications of teleoperation and motor control.

## Acknowledgments

The authors would like to thank Arno Stienen for his contributions in the early design stages of BROS, Mattia d'Alessi for his help in collecting the data of the human-human interaction experiment and Hankamp Rehab for their support in building the devices.

## References

- [1] J Meuleman, E van Asseldonk, G van Oort, H Rietman, and H van der Kooij. LOPES II - Design and Evaluation of an Admittance Controlled Gait Training Robot with Shadow-Leg Approach. *IEEE Transactions on Neural Systems and Rehabilitation Engineering*, 24(3):352–363, March 2016.
- [2] T Nef, M Mihelj, and R Riener. ARMin: A robot for patient-cooperative arm therapy. *Medical and Biological Engineering and Computing*, 45(9):887–900, September 2007.
- [3] A Melendez-Calderon, L Bagutti, B Pedrono, and E Burdet. Hi5: a versatile dual-wrist device to study human-human interaction and bimanual control. In *2011 IEEE/RSJ International Conference on Intelligent Robots and Systems*, pages 2578–2583. IEEE, 2011.
- [4] I S Howard, J N Ingram, and D M Wolpert. A modular planar robotic manipulandum with end-point torque control. *Journal of Neuroscience Methods*, 181(2):199–211, July 2009.
- [5] S H Scott. Apparatus for measuring and perturbing shoulder and elbow joint positions and torques during reaching. *Journal of Neuroscience Methods*, 89(2):119–127, 1999.
- [6] M Casadio, V Sanguineti, P G Morasso, and V Arrichiello. Braccio di Ferro: A new haptic workstation for neuromotor rehabilitation. *Technology and Health Care*, 14(3):123–142, September 2006.
- [7] H Gomi and M Kawato. Human arm stiffness and equilibrium-point trajectory during multi-joint movement. *Biological Cybernetics*, 76(3):163–171, March 1997.
- [8] R Q van der Linde, P Lammertse, E Frederiksen, and B Ruiter. The HapticMaster, a new high-performance haptic interface. *Proceedings of Eurohaptics*, pages 1–5, 2002.
- [9] J Klein, N Roach, and E Burdet. 3DOM: a 3 degree of freedom manipulandum to investigate redundant motor control. *IEEE Transactions on Haptics*, 7(2):229–239, April 2014.
- [10] G Ganesh, A Takagi, R Osu, T Yoshioka, M Kawato, and E Burdet. Two is better than one: Physical interactions improve motor performance in humans. *Scientific Reports*, 4, 2014.
- [11] A Takagi, G Ganesh, T Yoshioka, M Kawato, and E Burdet. Physically interacting individuals estimate the partner’s goal to enhance their movements. *Nature Human Behaviour*, 1(3):0054, 2017.
- [12] A Melendez-Calderon, V Komisar, and E Burdet. Interpersonal strategies for disturbance attenuation during a rhythmic joint motor action. *Physiology & Behavior*, 147:348–358, 2015.
- [13] N Beckers, A Q L Keemink, E van Asseldonk, and H van der Kooij. Haptic Human-Human Interaction Through a Compliant Connection Does Not Improve Motor Learning in a Force Field. In D Prattichizzo, H Shinoda, H Z Tan, E Ruffaldi, and A Frisoli, editors, *11th International Conference, EuroHaptics 2018*, pages 333–344. Springer International Publishing, 2018.
- [14] Y Che, G M Haro, and A M Okamura. Two is not always better than one: Effects of teleoperation and haptic coupling. *2016 6th IEEE ...*, pages 1290–1295, 2016.

- [15] J Diedrichsen. Optimal task-dependent changes of bimanual feedback control and adaptation. *Current Biology*, 17(19):1675–1679, 2007.
- [16] D A Braun, P A Ortega, and D M Wolpert. Nash equilibria in multi-agent motor interactions. *PLoS Computational Biology*, 5(8):e1000468, August 2009.
- [17] D M Wolpert, J Diedrichsen, and J R Flanagan. Principles of sensorimotor learning. *Nature Reviews Neuroscience*, 12(12):739–751, November 2011.
- [18] C M Gosselin and J Angeles. The Optimum Kinematic Design of a Planar Three-Degree-of-Freedom Parallel Manipulator. *Journal of Mechanisms Transmissions and Automation in Design*, 110(1):35, 1988.
- [19] J-P Merlet. *Parallel Robots*. Springer Science & Business Media, January 2006.
- [20] A Codourey. Dynamic modeling of parallel robots for computed-torque control implementation. *International Journal of Robotics Research*, 17(12):1325–1336, December 1998.
- [21] B Siciliano, L Sciavicco, L Villani, and G Oriolo. *Robotics; Modelling, Planning and Control*. Springer Science & Business Media, London, January 2009.
- [22] A Q L Keemink, H van der Kooij, and A H A Stienen. Admittance control for physical human–robot interaction. *International Journal of Robotics Research*, 1(2):027836491876895–24, April 2018.
- [23] P Lammertse. Admittance control and impedance control - a dual, with an application to master slave telemanipulation. Technical report, MOOG, November 2009.
- [24] J Werkmeister and A Slocum. Theoretical and experimental determination of capstan drive stiffness. *Precision Engineering*, 31(1):55–67, December 2006.
- [25] G Ellis. Cures for low-frequency mechanical resonance in industrial servo systems. *Conference Record of the IEEE Industry Applications Conference. th IAS Annual Meeting Cat. No.CH*, 1:252–258, 2001.
- [26] P M T Zaal, D M Pool, M Mulder, and M M van Paassen. Multimodal pilot control behavior in combined target-following disturbance-rejection tasks. *Journal of Guidance, Control, and Dynamics*, 32(5):1418–1428, September 2009.
- [27] F Janabi-Sharifi, V Hayward, and C-S J Chen. Discrete-time adaptive windowing for velocity estimation. *IEEE Transactions on Control Systems Technology*, 8(6):1003–1009, 2000.
- [28] L Simmatis, J Krett, S H Scott, and A Y Jin. Robotic exoskeleton assessment of transient ischemic attack. *PLoS ONE*, 12(12), December 2017.
- [29] T C Bourke, C R Lowrey, S P Dukelow, S D Bagg, K E Norman, and S H Scott. A robot-based behavioural task to quantify impairments in rapid motor decisions and actions after stroke. *Journal of NeuroEngineering and Rehabilitation*, pages 1–13, October 2016.